Int J Adv Manuf Technol (2016) 82:1595–1605
DOI 10.1007/s00170-015-7494-3

ORIGINAL ARTICLE

The multi-objective robust optimization of the loading path in the T-shape tube hydroforming based on dual response surface model

Tianlun Huang [1] · **Xuewei Song** [1] · **Xinyang Liu** [2]

Received: 25 January 2015 / Accepted: 22 June 2015 / Published online: 9 July 2015

Abstract In this study, a dual response surface model-based multi-objective robust optimization method is introduced to deal with the uncertainties in the tube hydroforming process. The objective of this study is to maximize the protrusion height and minimize the thinning ratio; meanwhile, the variations of the objectives should be minimized. A valid finite element model obtained from experimental result and LS-DYNA is employed to simulate the T-shape tube hydroforming process. To improve computation efficiency, radial basis function combined with Latin hypercube and orthogonal design sampling strategies is employed to construct dual response surface model, which are the mean and standard deviation response of the hydroforming process, respectively. The robust Pareto solutions can be obtained using NSGA-II; meanwhile, the ideal point method is used to obtain the most satisfactory solution from the Pareto solutions for the design engineers. As a conclusion, a significant improvement of the robustness can be achieved; however, the mean performance of the protrusion height has to be sacrificed.

Keywords Tube hydroforming · Loading path · Multi-objective robust optimization · Dual response surface model

✉ Tianlun Huang
huang_tianlun@126.com

Xuewei Song
sxwjlu@163.com

Xinyang Liu
xxl428@case.edu

1 State Key Laboratory of Automobile Dynamic Simulation, Jilin University, Changchun 130025, People's Republic of China

2 Case Western Reserve University, 10900 Euclid Ave., Cleveland, OH 44106, USA

1 Introduction

Tube hydroforming (THF) process has been widely used in the automotive and aircraft as well as sanitary industries in recent years due to its advantages as compared to conventional manufacturing via stamping and welding. These advantages include part consolidation, weight reduction, the increase of the strength and stiffness, the decrease of the workpiece cost and tooling cost, more uniform thickness distribution, etc. [1, 2].

THF is a complex metal forming process that involves material properties, geometric characteristics, and process parameters, such as strength coefficient, initial tube thickness, and friction coefficient, etc. Extensive research has been performed analytically, numerically as well as experimentally to analyze the effect of the material properties, geometric characteristics, and loading parameters on the forming quality [3–8]. Yang et al. [9] investigated the effect of the loading path on the forming result and gave a reasonable range of the loading path in THF process. Hwang et al. [10] conducted a series of experiment to test the effect of different loading paths on the formed parts, and they pointed out that the branch heights of the formed products with and without a counter punch were also compared to manifest the merit of using a counter punch during tube hydroforming. Alaswad et al. [11] compared the results, such as protrusion height, thickness distribution, and so on, between single and bi-layered THF process under the same conditions. Due to the complexity of the THF process, the loading path should be optimized to better control the process and guarantee the hydroformed parts with desired specification.

During the past decades, a number of papers have been published to search for the optimal loading path in the THF process. Yang et al. [12] dealt with sensitivities analysis and optimal process design of the THF process using the finite

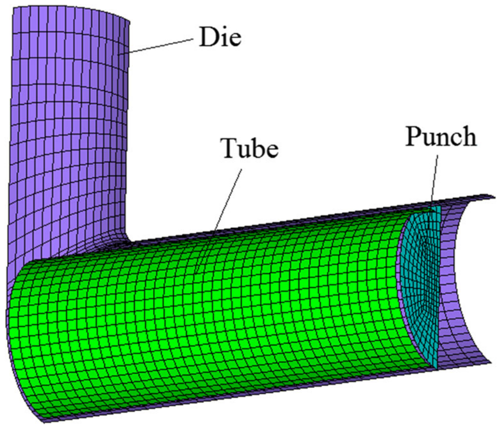

Fig. 1 A quarter of the FE model used for numerical simulation

element method (FEM) combined with an optimization tool. Fann and Hsiao [13] proposed an optimization strategy based on conjugate gradient method and FEM to determine the optimal loading path in the THF process, and they also pointed out that the loading path generated by sequential mode is better than that generated by the batch mode. Li et al. [14] developed a method to analyze the effect of the material properties, geometric characteristics, and loading parameters on the product quality using Taguchi method and FEM, and the optimal combination of the internal pressure and the friction coefficient was obtained by using goal attainment method. Ben and EI [15] provided a deep comparison between the quadratic polynomial response surface (RS) model and radial basis function (RBF) as surrogate techniques to construct surrogate models for global sensitivities and multi-objective optimization of the THF process, and they found that the RBF showed its superiority over the quadratic polynomial RS model to deal with nonlinearities proved through analytical test function and practical THF process. An et al. [16–18] used a multi-objective optimization algorithm combined with design of experiment (DOE) and FEM to determine the optimal loading path in the THF process. Kadkhodayan and Moghadam [19, 20] established a new method to optimize the loading parameters in the T-, X-, Y-shape THF process based on Taguchi method and the RS model. Aue-U-Lan et al. [21] studied the self-feeding and the adaptive simulation techniques as the optimization strategies to optimize the loading parameters. Mirzaali et al. [22, 23] used the simulated annealing algorithm to find the loading parameters in the THF process. Abedrabbo et al. [24] optimized the loading path in the THF process with experimental verification. Li et al. [25] proposed an adaptive simulation approach integrated with a fuzzy logic control algorithm to maximize the protrusion height for the T-shape THF process, and they used the forming limit curve and a simple geometry method to predict the necking and wrinkling. Teng et al. [26] optimized the loading paths for T-shape THF process based on a fuzzy control algorithm and FEM, and the result was validated against the experimental work. Manabe et al. [27] used an intelligent technique to determine the optimal loading paths for the T-shape THF process with a counter punch. Di Lorenzo et al. [28] proposed a gradient decomposition method, which aimed to reduce the number of the evaluations of the FE simulation, to optimize the internal pressure and counter punch action in Y-shape THF process. Ingarao et al. [29] applied the RS model and Pareto optimal solution search techniques to design a complex Y-shape THF process. Imaninejad et al. [30] discussed the effect of single-, double-, and quadruple-stroke axial displacement on the optimal results and the influence of the use of high and low internal pressure on the thickness variation.

The aforementioned strategies have been successfully applied for optimizing the THF process; however, most practical THF processes involve some degree of uncertainties in the material properties, geometric characteristics, and process parameters. It must be noted that usually, a deterministic optimization tends to push a design toward one or more constraints until the constraints become active, thereby leaving very little or no room for tolerances in modeling, uncertainties, and/or manufacturing imperfections. Therefore, the design could become misleading or even unacceptable when considering the perturbations of the design variables or the uncertainties of the process parameters. To tackle this problem, some progresses have been developed to deal with the uncertainties in the THF process [31–37]. Li et al. [31–33] studied the reliability of the THF process based on the stochastic frame and fuzzy programming. Abdessalem et al. [34] increased the stability of the THF process under stochastic frame. Ben et al. [35] discussed the reliability-based design optimization of the THF process. Kim et al. [36, 37] proposed a statistical approach to evaluate forming limit diagram based on first-order reliability method, Monte Carlo simulations, and Hill plastic instability criteria.

It can be seen from the literature review, there have been few reports available regarding multi-objective robust optimization of the loading path in the THF process. In this study, a multi-objective optimization method based on the dual RS model is introduced to deal with the uncertainties in the T-shape THF process. The remainder of paper is organized as follows: In Section 2, the FE model is presented and validated

Table 1 The geometric characteristics of the FE model

Tube length(mm)	Tube outer diameter(mm)	Tube thickness(mm)	Die corner radius(mm)	Branch tube diameter(mm)
121	24	1.3	3	24

Table 2 The material properties of the tube

Yield stress (MPa)	Density (kg/m^3)	Poisson's ratio	Young's modulus (GPa)	Strength coefficient (MPa)	Hardening exponent
116.37	8900	0.31	119.86	425.7	0.2562

against the experimental results. The dual RS model, which are the mean and standard deviation response of the hydroforming process, respectively, combined with Latin hypercube and orthogonal design sampling strategies is introduced in Section 3. Multi-objective robust optimization problem is formulated and the obtained results are analyzed and discussed in Section 4. Section 5 draws some conclusions on the presented work and future research direction are proposed.

2 FE model validated against the experimental results

2.1 FE Model

Due to the symmetric character of the T-shape THF process, only a quarter of the model is used to simulate the T-shape THF process and the nodes at the symmetry edges are restrained in the appropriate directions. Figure 1 shows a quarter of the model. It is composed of the die which represents the final desired part, the punch, which has the role of bringing matter to the expand zone at the end and avoid the premature plastic instability of the tube, and the tube. The total model is composed of 2256 shell elements. The tube is modeled using 4800 Belytschko-Tsay elements with five integration points through thickness, and the die and the punch are modeled as rigid bodies. The explicit dynamic FE code LS-DYNA [38] is adopted to simulate the T-shape THF process; a coulomb friction coefficient of 0.15 is used to simulate the friction behavior between the contact surface of the tube and the die. The geometric characteristics of the FE model are listed in Table 1.

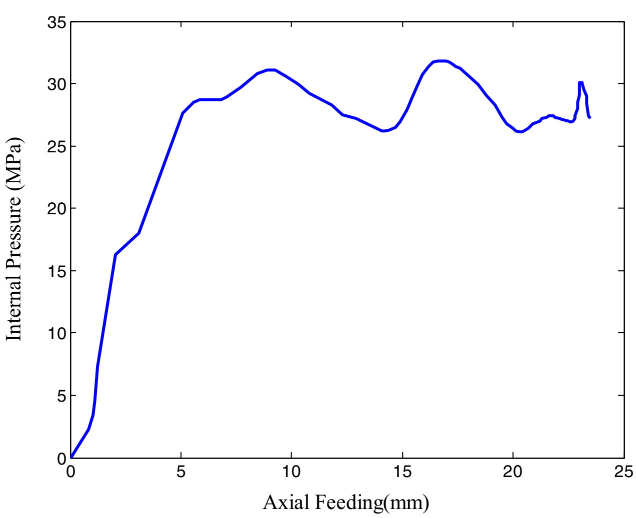

Fig. 2 The loading path used in the FE simulation

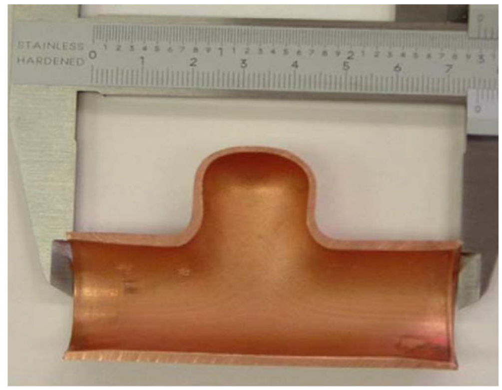

Fig. 3 The experimental result

2.2 Material properties

The annealed copper tubes are used to manufacture the T-shape tube part; Swift hardening law is adopted to characterize the material behavior

$$\overline{\sigma} = K\overline{\varepsilon}^{n} \tag{1}$$

where $\overline{\sigma}$ and $\overline{\varepsilon}$ are the effective stress and effective strain, respectively, K is the strength coefficient, and n is the strain hardening exponent. The material properties are shown in Table 2 [39].

2.3 The definition of the loading path

The loading path (the internal pressure versus the axial feeding) used for the THF process simulation is set according to the experimental procedures [39]. The maximum axial feeding is 23.5 mm. The loading path used in the FE simulation is shown in Fig. 2, and the simulation time is set to 0.01 s.

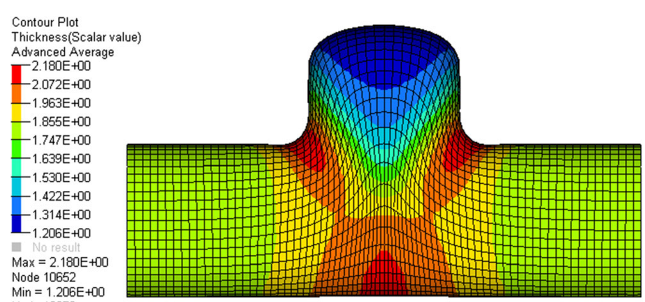

Fig. 4 The simulation result

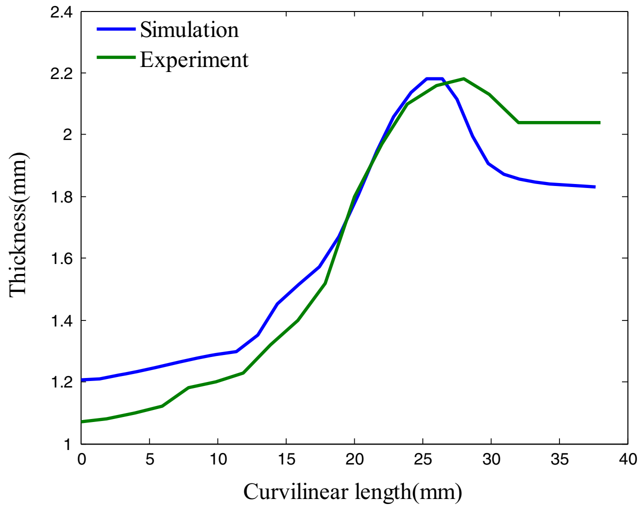

Fig. 5 The wall thickness distribution along the curvilinear length

2.4 The result validated against the experiment

Figures 3 and 4 show the wall thickness distribution of the experiment and the simulation, and Fig. 5 shows the wall thickness distribution of the experiment and the simulation in *zy*-plane along the curvilinear length of the tube. The wall thickness plot at the end of the tube is ignored due to the presence of the punch, and the definition of the curvilinear length can be referred to reference [39]. From Figs. 3, 4 and 5, it can be found that the simulation result shows a good agreement with the experimental result. Besides, the protrusion height of the experiment and simulation are 17.7 and 17.07 mm, respectively, and the relative error is −3.56 %. The protrusion height comparison also indicates that the accuracy of the FE model is acceptable. Thus, the FE model can be used for the optimization of the loading path in the THF process. It should be pointed out that the difference between the experimental and simulation results may be due to the boundary condition during the THF process, the error in measurement of the wall thickness and the inaccuracy of the material properties.

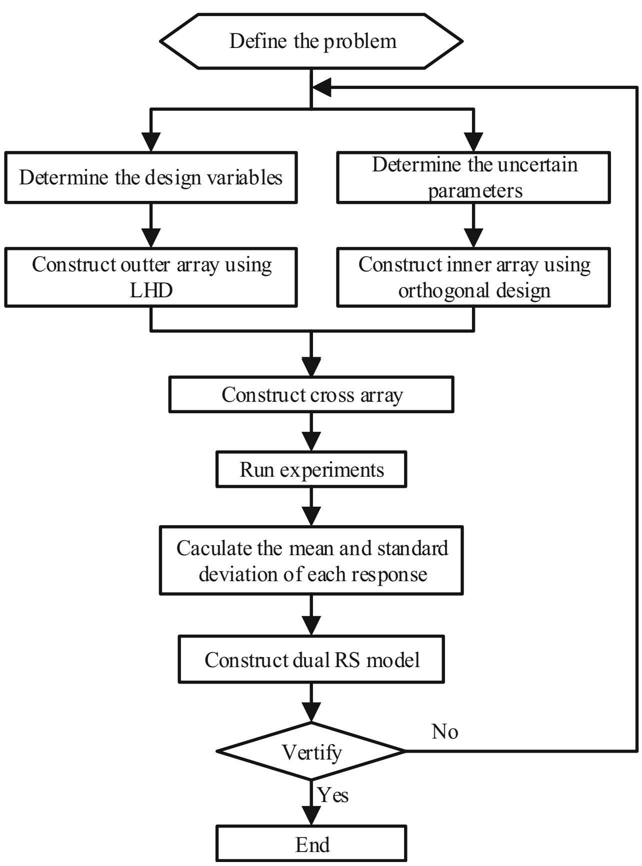

Fig. 6 The flow chart of constructing dual RS model

Table 3 The cross array design

				Inner array				
				U_1	1	1	……	3
				U_2	1	2	……	3
				U_3	1	2	……	2
				U_4	1	2	……	1
Outer array	X_1	X_2	X_3					
	13	1	5		$f_{1,1}$	$f_{1,2}$	…	$f_{1,9}$
	4	9	13		$f_{2,1}$	$f_{2,2}$	…	$f_{2,n}$
	…	…	…		…	…		…
	12	18	2		$f_{20,1}$	$f_{20,2}$	…	$f_{20,9}$

3 The dual RS model combined with DOE

The optimization of loading path in the THF process often requires large computational time, even when using reduced FE model. Implicit functions have to be evaluated for many times to explore the search space. To save the computation time, the use of the RS model is a preferable strategy. However, the conventional RS model only focuses on the mean value of the response without considering the variance. Therefore, only constructing mean response model may not be adequate and an optimization could become misleading [40]. While dual RS model allows constructing two models, the mean $\tilde{f}^{\mu}(\mathbf{x})$ and standard deviation $\tilde{f}^{\sigma}(\mathbf{x})$ of the response of the system is

$$\begin{aligned}\tilde{f}^{\mu}(\mathbf{x}) &= \sum a_i \phi_i(\mathbf{x}) \\ \tilde{f}^{\sigma}(\mathbf{x}) &= \sum b_i \varphi_i(\mathbf{x})\end{aligned} \tag{2}$$

Table 4 The ranges of loading parameters

	P_1(MPa)	P_2(MPa)	D(mm)
Lower bound	30	40	20
Upper bound	40	46	26

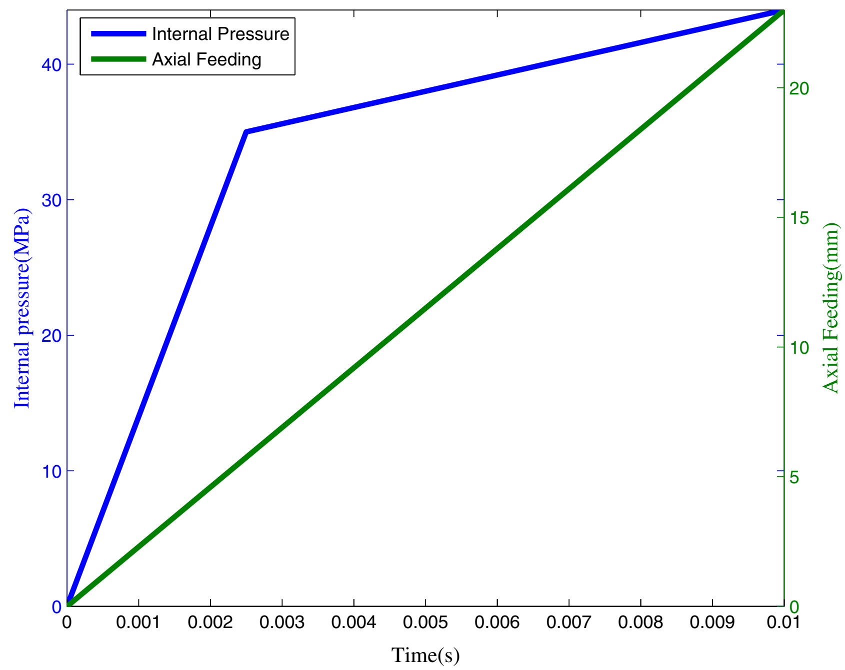

Fig. 7 The preliminary loading path

3.1 RBF model

Jin et al. [41] systematically compared several popular surrogate techniques, namely polynomial regression, kriging method, multivariate adaptive regression splines, and RBF; they pointed out that RBF performs the best when both average accuracy and robustness are considered. Hence, the RBF is used to construct the dual RS model. RBF [41] has been developed for the interpolation of scattered multivariate data. This method uses linear combinations of radially symmetric functions based on the Euclidean distance or other such metric. A RBF model can be expressed as

$$\tilde{f}(\mathbf{x}) = \sum_{j=1}^{N} w_j h(r_{\bullet j}) \quad (3)$$

where w_j represents the unknown coefficients, N is the number of the sampling points, h is the radial basis function, and $r_{\bullet j}=\|\mathbf{x}-\mathbf{x}_j\|$ represents the Euclidean distance between the estimate point and the jth sampling point. Some of the most commonly used basis functions include linear, cubic, thin plate spline, multi-quadric, inverse multi-quadric, and Gaussian, etc. In this study, the Gaussian function is selected as the basis function due to its effectiveness in surrogate model

$$h(r) = e^{-cr^2} \quad (4)$$

where c is a constant to be optimized. At the ith sampling point $\mathbf{x}_i$, the predicted value can be expressed as

$$\tilde{f}(\mathbf{x}_i) = \sum_{j=1}^{n} w_j h(r_{ij}) \quad (5)$$

where r_{ij} denotes the Euclidean distance between the ith sampling point and the jth sampling point, and Eq. (5) can be transformed in matrix notation as follows:

$$\mathbf{f} = \mathbf{Hw} \quad (6)$$

where $\mathbf{H}$ is a matrix:

$$\mathbf{H} = \begin{bmatrix} h(r_{11}) & h(r_{12}) & \cdots & h(r_{1N}) \\ h(r_{21}) & h(r_{22}) & \cdots & h(r_{2N}) \\ \vdots & \vdots & \ddots & \vdots \\ h(r_{N1}) & h(r_{N2}) & \cdots & h(r_{NN}) \end{bmatrix} \quad (7)$$

If the inverse of $\mathbf{H}$ exits, the unknown coefficient vector can be obtained as

$$\mathbf{w} = \mathbf{H}^{-1}\mathbf{f} \quad (8)$$

It has been proven that the matrix $\mathbf{H}$ is always invertible for arbitrary scattered sampling points [42].

Table 5 The ranges of uncertain parameters

	K(MPa)	n	μ	t_0(mm)
Lower bound	383.13	0.23058	0.135	1.17
Upper bound	468.27	0.28182	0.165	1.43

3.2 DOE

When using the RBF model to construct dual RS model, the sampling points should be carefully located. In this study, the

Latin hypercube design (LHD) [43] method is selected to locate the outer sampling points, while the orthogonal design is used to collect the inner sampling points. The flow chart [44] of constructing dual RS model is shown in Fig. 6. The calculation of the dual RS model can be described as follows:

Step 1 Define the problem and determine the design variables and the uncertain parameters.

Step 2 Construct the cross array to locate the sampling points, where the design variables are arranged in the outer array while the uncertain parameters are arranged in the inner array. As an example shown in Table 3, LHD is used to locate 20 sampling points of design variables and orthogonal design is used to collect 9 sampling points of uncertain parameters.

Step 3 Run experiments using numerical simulations, such as FEM. It should be noted that each experiment at outer array is repeated 9 times corresponding to the inner array to simulate the mean and standard deviation due to the uncertain parameters. As is shown in Table 3, $f_{i,j}$ is the response at ith row of the outer array and jth column of the inner array.

Step 4 Calculate the mean and standard deviation of the response according to Eq. 9:

$$\begin{aligned} f_i^{\mu}(x) &= \frac{1}{n}\sum_{j=1}^{n} f_{i,j}(x) \\ f_i^{\sigma}(x) &= \sqrt{\frac{1}{n-1}\sum_{j=1}^{n}\left(f_{i,j}(x)-f_i^{\mu}(x)\right)^2} \end{aligned} \tag{9}$$

where $f_i^{\mu}(x)$ and $f_i^{\sigma}(x)$ are the mean and standard deviation of the response at the ith sampling point in the outer array, n is the number of the sampling points in the inner array.

Step 5 Construct the dual RS model according the Eqs. (2)–(8).

Step 6 Evaluating the performance of the dual RS model according Eq. (10) and Eq. (11):

$$\mathrm{MRE} = \mathrm{Max}\left|\frac{\tilde{f}_i - f_i}{f_i}\right| \times 100\% \tag{10}$$

$$R^2 = 1 - \frac{\sum_{i=1}^{N}\left(f_i - \tilde{f}_i\right)^2}{\sum_{i=1}^{N}\left(f_i - \bar{f}_i\right)^2} \tag{11}$$

Table 6 The protrusion height of the FE simulation

Design variables				Uncertain parameters									
				K	383.13	383.13	383.13	425.70	425.70	425.70	468.27	468.27	468.27
				n	0.2306	0.2562	0.2818	0.2306	0.2562	0.2818	0.2306	0.2562	0.2818
				t_0	1.17	1.30	1.43	1.43	1.17	1.30	1.30	1.43	1.17
No.	P_1	P_2	D	μ	0.135	0.150	0.165	0.150	0.165	0.135	0.165	0.135	0.150
1	39.14	40.26	23.27		22.698	21.126	19.849	18.57	21.149	19.803	18.612	17.734	19.941
2	32.46	42.00	23.38		21.479	20.098	18.978	17.863	20.121	18.954	17.879	17.041	19.075
3	37.46	44.88	25.11		24.34	22.653	21.221	19.849	22.636	21.168	19.903	18.958	21.313
4	30.45	42.97	21.46		20.224	18.918	17.779	16.68	18.91	17.735	16.696	15.955	17.862
5	36.43	41.74	24.78		23.125	21.599	20.397	19.135	21.618	20.352	19.209	18.311	20.484
6	30.71	40.56	20.61		19.224	17.989	16.984	15.886	17.979	16.928	15.895	15.23	17.049
7	33.52	43.13	22.58		21.473	20.055	18.926	17.654	20.062	18.876	17.685	16.895	18.984
8	33.18	41.48	24.40		22.095	20.726	19.523	18.405	20.725	19.511	18.425	17.662	19.67
9	35.02	44.78	22.71		22.31	20.747	19.471	18.156	20.735	19.405	18.193	17.288	19.535
10	36.84	43.56	20.28		21.033	19.52	18.244	16.956	19.522	18.209	16.983	16.123	18.329
11	34.51	40.61	21.63		20.573	19.242	18.106	16.97	19.237	18.069	16.998	16.251	18.179
12	39.57	42.49	22.38		22.771	21.101	19.756	18.412	21.128	19.709	18.453	17.534	19.847
13	32.54	45.41	22.06		21.581	20.064	18.859	17.507	20.056	18.802	17.545	16.75	18.918
14	38.46	43.71	24.91		24.2	22.48	21.12	19.763	22.488	21.077	19.805	18.833	21.22
15	31.30	44.21	21.14		20.461	19.074	17.895	16.74	19.067	17.854	16.737	15.918	17.969
16	31.65	44.18	24.16		22.326	20.859	19.599	18.412	20.841	19.579	18.44	17.661	19.721
17	34.39	42.13	25.44		23.069	21.61	20.426	19.219	21.633	20.389	19.249	18.413	20.522
18	35.73	45.24	25.73		24.341	22.669	21.273	19.937	22.659	21.237	19.986	19.104	21.409
19	37.93	41.08	20.44		20.8	19.336	18.138	16.868	19.354	18.091	16.894	16.069	18.208
20	38.93	45.74	23.69		24.106	22.28	20.869	19.354	22.292	20.812	19.403	18.475	20.95

where MRE is the maximum relative error between the predicted response and the actual response, R^2 is the coefficient of the determination, f is the actual mean or standard deviation of the response, $\tilde{f}$ is the predicted value and $\overline{f}$ is the average value. N is the number of the sampling points in the outer array. Generally speaking, the smaller the MRE and the larger the R^2, the better the performance of the dual RS model can be obtained.

Step 7 Repeating the steps above until the errors become acceptable.

4 Multi-objective robust optimization

In the T-shape THF process, there are several, possibly conflicting, objectives, such as the maximum thinning ratio and the protrusion height. Therefore, all the objectives cannot be simultaneously optimized. For instance, for typical T-shape THF process, the maximum thinning ratio and the protrusion height are two competing objectives; there is a need to maximize the protrusion height while the maximum thinning ratio maintaining a reasonable value. Besides, uncertainties associated with material properties, geometric characteristics, and loading parameters widely exist in the actual THF process. Therefore, it is necessary to introduce a multi-objective robust optimization method to deal with the uncertainties in the THF process.

4.1 The definition of the objectives

In the T-shape THF process, the primary objective is to manufacture the part with the maximum protrusion height without any failure happening. Among three main failure modes, namely bursting, wrinkling, and buckling, involved in the THF process, bursting failure is irrevocable while other failures are revocable [45]. Although there are many different criteria for predicting bursting in the THF process, there is no clearly a preferred approach. In this study, the maximum thinning ratio is used as a measure of product quality. The maximum thinning ratio can be defined as follows:

$$\text{Thinning ratio}(\%) = \frac{t_0 - t_{\min}}{t_0} \times 100\% \tag{12}$$

where t_0 is the initial tube thickness and $t_{\min}$ is the minimum thickness of the final hydroformed parts. As

Table 7 The maximum thinning ratio of the FE simulation

Design variables				Uncertain parameters									
				K	383.13	383.13	383.13	425.70	425.70	425.70	468.27	468.27	468.27
				n	0.2306	0.2562	0.2818	0.2306	0.2562	0.2818	0.2306	0.2562	0.2818
				t_0	1.17	1.30	1.43	1.43	1.17	1.30	1.30	1.43	1.17
No.	P_1	P_2	D	μ	0.135	0.150	0.165	0.150	0.165	0.135	0.165	0.135	0.150
1	39.14	40.26	23.27		16.942	14.115	11.474	6.891	14.004	11.390	7.073	6.290	11.762
2	32.46	42.00	23.38		14.232	11.906	9.771	5.901	11.950	9.715	6.151	5.348	10.074
3	37.46	44.88	25.11		19.258	15.652	12.592	7.533	15.241	12.325	7.695	6.811	12.676
4	30.45	42.97	21.46		15.124	12.520	10.087	5.987	12.461	10.023	6.328	5.453	10.471
5	36.43	41.74	24.78		15.331	12.766	10.676	6.371	12.757	10.600	6.732	5.885	10.898
6	30.71	40.56	20.61		12.831	10.857	8.870	5.254	10.828	8.875	5.493	4.755	9.325
7	33.52	43.13	22.58		15.829	13.117	10.831	6.351	13.106	10.770	6.618	5.803	11.044
8	33.18	41.48	24.40		13.904	11.754	9.595	5.833	11.613	9.544	5.980	5.321	9.979
9	35.02	44.78	22.71		18.418	14.953	12.174	7.211	14.786	11.999	7.391	6.452	12.212
10	36.84	43.56	20.28		18.272	15.184	12.261	7.197	15.015	12.131	7.426	6.523	12.540
11	34.51	40.61	21.63		14.185	11.828	9.711	5.917	11.863	9.756	6.121	5.518	10.095
12	39.57	42.49	22.38		19.067	15.648	12.757	7.564	15.542	12.609	7.794	6.926	12.922
13	32.54	45.41	22.06		18.882	15.043	12.178	6.968	14.897	12.006	7.271	6.374	12.265
14	38.46	43.71	24.91		18.508	15.109	12.340	7.436	14.918	12.090	7.588	6.720	12.453
15	31.30	44.21	21.14		16.970	13.776	11.043	6.632	13.707	11.025	6.753	5.804	11.413
16	31.65	44.18	24.16		16.780	13.711	10.998	6.428	13.439	10.771	6.678	5.956	11.166
17	34.39	42.13	25.44		14.613	12.324	10.279	6.161	12.240	10.083	6.360	5.594	10.379
18	35.73	45.24	25.73		18.881	15.311	12.235	7.207	14.905	11.973	7.523	6.680	12.423
19	37.93	41.08	20.44		16.999	14.242	11.623	6.820	14.219	11.560	7.004	6.243	11.873
20	38.93	45.74	23.69		21.603	17.026	13.783	8.073	16.884	13.508	8.212	7.345	13.881

Table 8 The actual and normalized values of mean and the standard deviation of the protrusion height and the maximum thinning ration

Design variables				Actual values				Normalized values			
No.	P_1	P_2	D	f_h^μ	f_h^σ	f_t^μ	f_t^σ	f_h^μ	f_h^σ	f_t^μ	f_t^σ
1	39.14	40.26	23.27	19.9425	1.5413	11.1045	3.6977	0.5485	0.5133	0.5193	0.4717
2	32.46	42.00	23.38	19.0542	1.3684	9.4498	3.0824	0.4608	0.3427	0.3508	0.3279
3	37.46	44.88	25.11	21.3380	1.6738	12.1982	4.2204	0.6864	0.6441	0.6306	0.5939
4	30.45	42.97	21.46	17.8623	1.3326	9.8282	3.3333	0.3431	0.3074	0.3893	0.3865
5	36.43	41.74	24.78	20.4699	1.4873	10.2241	3.2717	0.6006	0.4600	0.4296	0.3721
6	30.71	40.56	20.61	17.0184	1.2490	8.5654	2.8340	0.2598	0.2249	0.2608	0.2698
7	33.52	43.13	22.58	18.9566	1.4287	10.3855	3.4775	0.4512	0.4022	0.4461	0.4202
8	33.18	41.48	24.40	19.6379	1.3844	9.2804	3.0010	0.5185	0.3585	0.3336	0.3089
9	35.02	44.78	22.71	19.5379	1.5565	11.7327	4.0631	0.5086	0.5283	0.5832	0.5571
10	36.84	43.56	20.28	18.3245	1.5306	11.8390	4.0726	0.3887	0.5028	0.5940	0.5593
11	34.51	40.61	21.63	18.1806	1.3496	9.4438	3.0312	0.3745	0.3241	0.3502	0.3159
12	39.57	42.49	22.38	19.8568	1.6257	12.3143	4.1807	0.5401	0.5966	0.6424	0.5846
13	32.54	45.41	22.06	18.8981	1.5120	11.7651	4.2421	0.4454	0.4844	0.5865	0.5989
14	38.46	43.71	24.91	21.2206	1.6557	11.9068	4.0149	0.6748	0.6262	0.6010	0.5458
15	31.30	44.21	21.14	17.9684	1.4094	10.7914	3.7844	0.3536	0.3832	0.4874	0.4920
16	31.65	44.18	24.16	19.7154	1.4563	10.6585	3.7211	0.5261	0.4294	0.4739	0.4772
17	34.39	42.13	25.44	20.5033	1.4446	9.7816	3.1405	0.6039	0.4179	0.3846	0.3415
18	35.73	45.24	25.73	21.4018	1.6317	11.9042	4.1567	0.6927	0.6025	0.6007	0.5790
19	37.93	41.08	20.44	18.1954	1.4755	11.1758	3.7770	0.3760	0.4484	0.5265	0.4902
20	38.93	45.74	23.69	20.9491	1.7542	13.3682	4.8078	0.6480	0.7234	0.7497	0.7311

mentioned above, the protrusion height and the maximum thinning ratio are usually two competing objectives. Thus, it forms a multi-objective optimization problem to optimize the protrusion height and the maximum thinning ratio.

4.2 The definition of the design variables and the uncertain parameters

A successful THF process depends on a number of factors, such as the loading path (internal pressure vs. time, the axial feeding vs. time), the lubrication condition, the geometric characteristics, and the material properties. Therefore, a suitable loading path is of great importance to guarantee the stability of the THF process. In this study, the variation of the internal pressure versus time is modeled by two points (P_1, P_2), and the axial feeding D is imposed as a linear function of time. The ranges of the loading parameters applied in the T-shape THF process are determined by running few numerical simulations, and the ranges of loading parameters are given in Table 4. The preliminary loading path is shown in Fig. 7.

In this study, the strength coefficient (K), strain hardening exponent (n), friction coefficient (μ), and tube thickness (t_0) are regarded as the uncertain parameters. The ranges of uncertain parameters are given in Table 5.

Table 9 Performance evaluation of the dual RS model

	f_h^μ	f_h^σ	f_t^μ	f_t^σ
R^2	0.9993	0.9937	0.9956	0.9710
MRE (%)	0.3119	1.0521	1.2739	4.4266

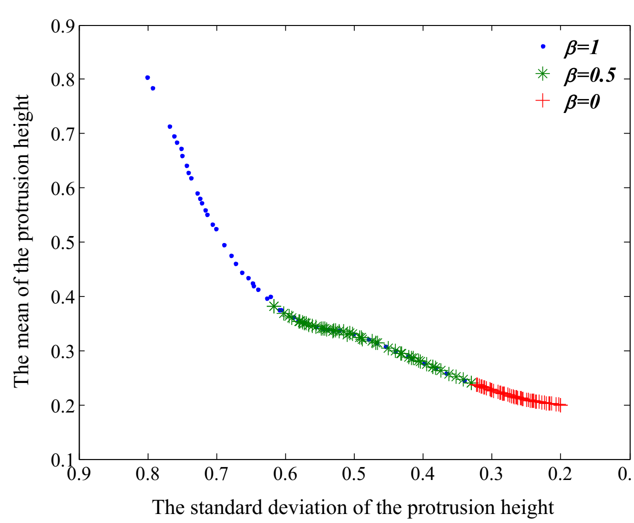

Fig. 8 Pareto frontiers of the protrusion height

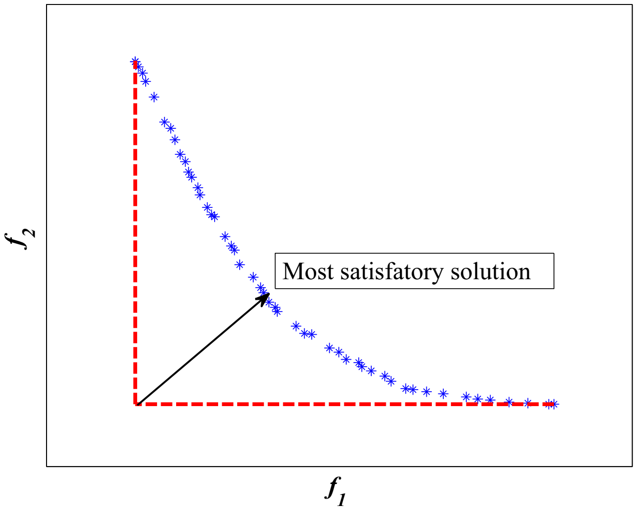

Fig. 9 The most satisfactory solution

4.3 The multi-objective robust optimization problem

From the above discussion, the multi-objective robust optimization problem can be formulated as follows:

$$\min_{\mathbf{x}_l \le \mathbf{x} \le \mathbf{x}_u,\, \mathbf{u}_l \le \mathbf{u} \le \mathbf{u}_u} \{f_{\mathrm{h}}(\mathbf{x},\mathbf{u}), f_{\mathrm{t}}(\mathbf{x},\mathbf{u})\} \tag{13}$$

where f_{h} and f_{t} are the protrusion height and the maximum thinning ratio, respectively. $\mathbf{x}_{\mathrm{l}}$ and $\mathbf{x}_{\mathrm{u}}$ denote the lower and upper bounds of the design variable $\mathbf{x}$, $\mathbf{u}_{\mathrm{l}}$ and $\mathbf{u}_{\mathrm{u}}$ denote the lower and upper bounds of the uncertain parameter $\mathbf{u}$.

The objective of manufacturing the part is to maximize protrusion height and minimize maximum thinning ratio; moreover, the variation of the objective should be as small as possible. Through the linear combination method, the Eq. (13) can be converted as follows:

$$\min_{\mathbf{x}_l \le \mathbf{x} \le \mathbf{x}_u} \left\{-\beta f_h^{\mu}(\mathbf{x}) + (1-\beta) f_h^{\sigma}(\mathbf{x}), \beta f_t^{\mu}(\mathbf{x}) + (1-\beta) f_t^{\sigma}(\mathbf{x})\right\} \tag{14}$$

where f_h^{μ} and f_h^{σ} are the mean and standard deviation of the protrusion height, f_t^{μ} and f_t^{σ} are the mean and standard deviation of the maximum thinning ratio, and β is the weight coefficient to emphasize the mean or standard deviation of the response. In this study, NSGA-II [46] is employed to solve Eq. (14). Because NSGA-II is a well-studied optimization algorithm, the description of the determination of the proper parameters for a NSGA-II operation can be referred to reference [46].

4.4 Result and discussion

The design variables located with LHD are arranged in an outer array with sampling points of 20. Experiments with orthogonal design are repeated nine times corresponding to the outer array to simulate the mean and standard deviation due to the uncertain parameters. The protrusion height and the maximum thinning ratio of the FE simulation results are listed in Tables 6 and 7. The mean and standard deviation of the protrusion height and the maximum thinning ratio are given in Table 8. In order to avoid numerical magnitude difference, all the mean and the standard deviation values are normalized to a dimensionless value between 0.2 and 0.8. The normalized value can be obtained according to Eq. (15):

$$\text{Normalized value} = 0.2 + (0.8-0.2) \times \frac{f^{\bullet} - f^{\bullet}_{\min}}{f^{\bullet}_{\max} - f^{\bullet}_{\min}} \tag{15}$$

where $f^{\bullet}$ is the mean or standard value of the protrusion height or the maximum thinning ratio and $f^{\bullet}_{\min}$ and $f^{\bullet}_{\max}$ are the corresponding minimum and maximum value. The normalized results are shown in Table 8. Based on the results in Table 8, RBF is employed to construct dual RS model, which, respectively, represents the mean and standard deviation.

Before optimizing the T-shape THF process, it is necessary to evaluate the performance of the dual RS model. In this study, the coefficient of the determination R^2 and maximum relative error (MRE) are used to evaluate the performance of the dual RS model. Because the RBF model is an interpolation, the performance evaluation of the dual RS model cannot be obtained from the interpolation points. Therefore, five extra sampling points are randomly selected to evaluate R^2 and MRE. Table 9 summarizes the error analysis results of R^2 and MRE. From Table 9, it can be found that the performance of the dual RS model is very good and allow us to carry out the design optimization properly.

Table 10 The most satisfactory solution

	f_h^{μ}	f_h^{σ}	f_t^{μ}	f_t^{σ}
β=0.5 Design variable = [30.26,40.01,24.30]	18.7949	1.2417	8.1233	2.6974
Verified by the FE simulations	19.0879	1.1866	8.069	2.5896
Relative error (%)	1.5350	−4.6435	−0.6729	−4.1628
β=1.0 Design variable = [35.37,40.16,25.98]	20.8979	1.3734	9.1517	2.9526
Verified by the FE simulations	20.7573	1.4232	9.2607	3.0525
Relative error (%)	-0.6727	3.4992	1.1914	3.9279

The population size of NSGA-II algorithm is 100, the maximum iterations is 100, the cross fraction is 0.8, the migration fraction is 0.2, and the Pareto population size is 50. Figure 8 presents the optimal Pareto frontiers of the mean and the standard deviation of the protrusion height for different weight coefficient β. It can be found that the small weight coefficient is set, the smaller standard deviation can be obtained, which means that the more robust solution can be achieved, the mean objective function becomes worse.

Although the Pareto solutions can provide design engineers with a number of design solutions for their decision making at the beginning step, the design engineers must make a decision from the Pareto solutions. In this study, the ideal point method [47] is used to obtain the most satisfactory solution. As

$$\min\ D = \sqrt{\sum_{i=1}^{M} \left(f^i - f^i_{\mathrm{best}}\right)^2} \tag{16}$$

where M is the number of the objectives, f^i is the ith objective function value, and f^i_{best} is the corresponding best value. The geometrical meaning of the most satisfactory solution is shown in Fig. 9.

As an example, the weight coefficient is set to 1 and 0.5; the most satisfactory solution is obtained using multi-objective robust optimization method and verified by FE simulations, and the results are listed in Table 10. It can be found that the results obtained using multi-objective robust optimization method showed a good agreement with that obtained from the FE simulations. The mean of protrusion height corresponding to β=1 is higher. In other words, when setting β=1, the maximum mean of the protrusion height of the Pareto solutions can be obtained, while, when setting β=0.5, a more robust mean of the protrusion height can be obtained. Therefore, to obtain a robust solution, a smaller weight coefficient is preferred. Besides, from Table 10, it can be observed that when a larger protrusion height is obtained, the maximum thinning ratio is also larger. It also indicates that the protrusion height and the maximum thinning ratio cannot be simultaneously optimized.

5 Conclusion

This study provides a multi-objective robust optimization method based on dual RS model to obtain the robust Pareto solutions for the T-shape THF process. To reduce computation time, RBF is employed to construct the dual RS model, and the accuracy of RBF is validated by five extra sampling points due to the interpolation nature of the RBF. From the results (Figs. 8 and 9), it can be found that the mean and the standard deviation cannot be optimized simultaneously. Generally, a more robust solution could sacrifice the mean performance of the T-shape THF process. Therefore, the design engineers should make a compromise between the mean and the standard deviation in practice. Finally, the ideal point method is introduced to help design engineers choose a most satisfactory solution from the Pareto solutions.

The direction of our future research is to consist in introducing other multi-objective robust optimization method, such as multi-objective robust optimization method based on interval analysis or convex model, to cope with limited information. This will be done to compare the advantages and disadvantages between the probability method and the non-probability method in dealing with the uncertainties in the THF process.

Acknowledgments This work is supported by National Natural Science Foundation of China (Grant No.51175218).

References

1. Ahmetoglu M, Altan T (2000) Tube hydroforming: state-of-the-art and future trends. J Mater Process Technol 98:25–33
2. Dohmann F, Hartl CH (1996) Hydroforming—a method to manufacture lightweight parts. J Mater Process Technol 60:669–676
3. Asnafi N (1999) Analytical modelling of tube hydroforming. Thin-Walled Struct 34:295–330
4. Asnafi N, Skogsgardh A (2000) Theoretical and experimental analysis of stroke-controlled tube hydroforming. J Mater Sci A279:95–110
5. Xu X, Li S, Zhang W, Lina Z (2009) Analysis of thickness distribution of square-sectional hydroformed parts. J Mater Process Technol 209:158–164
6. Manabe K, Amino M (2002) Effects of process parameters and material properties on deformation process in tube hydroforming. J Mater Process Technol 123:285–291
7. Carleer B, Kevie G, Winter L, Veldhuizen B (2000) Analysis of the effect of material properties on the hydroforming process of tubes. J Mater Process Technol 104:158–166
8. Fatemi A, Morovvati MR, Biglari FR (2013) The effect of tube material, microstructure, and heat treatment on process responses of tube hydroforming without axial force. Int J Adv Manuf Techonol 68:263–276
9. Yang B, Zhang W, Li SH (2006) Analysis and finite element simulation of the tube bulge hydroforming process. Int J Adv Manuf Techonol 29:453–458
10. Hwang YM, Lin TC, Chang WC (2007) Experiment on T-shape hydroforming with counter punch. J Mater Process Technol 192–193:243–248
11. Alaswad A, Benyounis KY, Olabi AG (2011) Finite element comparison of single and bi-layer tube hydroforming processes. Simul Model Pract Th 19:1584–1593
12. Yang JB, Heon BH, Sl O (2006) Design sensitivity analysis and optimization of the hydroforming process. J Mater Process Technol 113:666–672
13. Fann KJ, Hsiao PY (2003) Optimization of loading conditions for tube hydroforming. J Mater Process Technol 140:520–524
14. Li B, Nye TJ, Metzger DR (2006) Multi-objective optimization of forming parameters for tube hydroforming process based on the Taguchi method. Int J Adv Manuf Techonol 28:23–30
15. Abdessalem AB, Hami AE (2014) Global sensitivity analysis and multi-objective optimization of loading path in tube hydroforming

process based on metamodelling techniques. Int J Adv Manuf Techonol 71:753–773
16. An H, Green DE, Johrendt J (2010) Multi-objective optimization and sensitivity analysis of tube hydroforming. Int J Adv Manuf Techonol 50:67–84
17. An H, Green DE, Johrendt J (2012) A hybrid-constrained MOGA and local search method to optimize the load path for tube hydroforming. Int J Adv Manuf Techonol 60:1017–1030
18. An H, Green DE, Johrendt J (2013) Multi-objective optimization of loading path design in multi-stage tube forming using MOGA. Int J Mater Form 6:125–135
19. Kadkhodayan M, Moghadam AE (2012) An investigation of the optimal load paths for the hydroforming of T-shaped tubes. Int J Adv Manuf Techonol 61:73–85
20. Kadkhodayan M, Moghadam AE (2013) Optimization of load paths in X- and Y-shaped hydroforming. Int J Mater Form 6:75–91
21. Aue-U-Lan Y, Ngaile G, Altan T (2004) Optimizing tube hydroforming using process simulation and experimental verification. J Mater Process Technol 146:137–143
22. Mirzaali M, Seyedkashi SMH, Liaghat GH, Moslemi Naeini H, Shojaee K, Moon YH (2012) Application of simulated annealing method to pressure and force loading optimization in tube hydroforming process. Int J Mech Sci 55:78–84
23. Mirzaali M, Liaghat GH, Moslemi Naeini H, Seyedkashi SMH, Shojaee K (2011) Optimization of tube hydroforming process using simulated annealing algorithm. Procedia Eng 10:3012–3019
24. Abedrabbo N, Worswick M, Mayer R, Riemsdijk I (2009) Optimization methods for the tube hydroforming process applied to advanced high-strength steels with experimental verification. J Mater Process Technol 209:110–123
25. Li S, Yang B, Zhang W, Lin Z (2008) Loading path prediction for tube hydroforming process using a fuzzy control strategy. Mater Des 210:1110–1116
26. Teng B, Li K, Yuan S (2013) Optimization of loading path in hydroforming T-shape using fuzzy control algorithm. Int J Adv Manuf Techonol 69:1079–1086
27. Manabe K, Suetake M, Koyama H, Yang M (2006) Hydroforming process optimization of aluminum alloy tube using intelligent control technique. Int J Mach Tool Manuf 46:1207–1211
28. Di Lorenzo R, Ingarao G, Chinesta F (2009) A gradient-based decomposition approach to optimize pressure path and counter punch action in Y-shaped tube hydroforming operations. Int J Adv Manuf Technol 44:49–60
29. Ingarao G, Di Lorenzo R, Micari F (2009) Internal pressure counter punch action design in Y-shaped tube hydroforming processes: a multi-objective optimisation approach. Comput Struct 87:591–602
30. Imaninejad M, Subhash G, Loukus A (2005) Load path optimization of tube hydroforming process. Int J Mach Tools Manuf 45: 1504–1514
31. Li B, Metzger DR, Nye TJ (2006) Reliability analysis of the tube hydroforming process based on forming limit diagram. Trans ASME 128:402–407
32. Li B, Nye TJ, Metzger DR (2006) Improving the reliability of the tube-hydroforming process by the Taguchi method. Trans ASME 129:242–247
33. Li B, Metzger DR, Nye TJ (2004) Reliability analysis of the tube hydroforming process using fuzzy sets theory. Transactions of the ASME 11-17
34. Abdessalem AB, Pagnacco E, Hami AE (2013) Increasing the stability of T-shape tube hydroforming process under stochastic framework. Int J Adv Manuf Techonol 69:1343–1357
35. Ben Abdessalem A, El Hami A, Cherouat A (2010) Optimization of the tube hydroforming process using probabilistic constraints on failure modes. In: Proceedings of the tenth ICCST. Civil-Comp, Stirlingshire
36. Kim J, Kang BS, Lee JK (2009) Statistical evaluation of forming limit in hydroforming process using plastic instability combined with FORM. Int J Adv Manuf Techonol 42:53–59
37. Kim J, Song WJ, Kang BS (2009) Probabilistic modeling of stress-based FLD in tube hydroforming process. Int J Mech Sci 23:2891–2902
38. LS-DYNA (2006) Keyword user's manual, vol 971. Livermore Software Technology Corporation, Livermore
39. Ray P, Mac Donald BJ (2005) Experimental study and finite element analysis of simple X- and T-branch tube hydroforming processes. Int J Mech Sci 47:1498–1518
40. Yeniay O, Unal R, Lepsch RA (2006) Using dual response surfaces to reduce variability in launch vehicle design: a case study. Reliab Eng Syst Saf 97:407–412
41. Jin R, Chen W, Simpson TW (2001) Comparative studies of metamodeling techniques under multiple modeling criteria. Struct Multidisc Optim 23:1–13
42. Liu GR (2003) Mesh free methods: moving beyond the finite element method. CRC Press, Boca Raton
43. Jourdan A, Franco J (2010) Optimal Latin hypercube designs for the Kullback–Leibler criterion. AStA Adv Stat Anal 94:341–351
44. Sun G, Li G, Zhou S, Li H, Hou S, Li Q (2011) Crashworthiness design of vehicle by using multiobjective robust optimization. Struct Multidisc Optim 44:99–110
45. Yuan S, Yuan W, Wang X (2006) Effect of wrinkling behavior on formability and thickness distribution in tube hydroforming. J Mater Process Technol 177:668–671
46. Deb K, Pratap A, Agarwal S, Meyarivan T (2002) A fast and elitist multiobjective genetic algorithm: NSGA-II. IEEE Trans Evol Comput 6:182–197
47. Chen BL (2002) Optimization theories and algorithms. Tsinghua University Press, Beijing